Available online at www.sciencedirect.com

SCIENCE DIRECT®

Journal of Sound and Vibration 273 (2004) 989–1006

JOURNAL OF
SOUND AND
VIBRATION

www.elsevier.com/locate/jsvi

A coupled field study on the non-linear dynamic characteristics of an electrostatic micropump

T.Y. Ng[a,b,*], T.Y. Jiang[b], Hua Li[b], K.Y. Lam[b], J.N. Reddy[c]

[a] *School of Mechanical and Production Engineering, Nanyang Technological University, 50 Nanyang Avenue, Singapore 639798*

[b] *Institute of High Performance Computing, 1 Science Park Road, #01-01 The Capricorn Singapore Science Park II, Singapore 117528*

[c] *Department of Mechanical Engineering, Texas A&M University, College Station, TX 77843-3123, USA*

Received 27 November 2001; accepted 7 May 2003

Abstract

In this paper, a micropump actuated by electrostatic forces is dynamically analyzed. Coupled electro-mechanical effects are considered in the evaluation of the performance of the electrostatic micropump. The boundary element method is employed here to solve the quasi 3-D Laplace equation that the potential difference satisfies in order to obtain the surface charge density and corresponding electrostatic force. First order shear deformation theory is used to model the electrode membrane of the pump. Geometric non-linearity arises due to the inclusion of von Karman strains. The finite element method is employed to discretize the governing equations and Newton's iteration method is employed to solve the discretized equations. With the electro-mechanical coupling effects considered within the framework of linear plate theory, i.e., ignoring the von Karman strains, similar response trends are obtained for the 2-D plate analysis as that of 1-D analysis found in open literature. The present study is extended to non-linear analysis with von Karman strains included and non-linear load–deflection relationship is demonstrated. Variation of the amplitude and frequency of the potential difference applied across the two electrodes are investigated and responses are compared with those of linear analysis. Qualitatively different responses are observed. Also, the effects of the length-to-thickness ratio of the electrode plate are examined in detail.

---

*Corresponding author. School of Mechanical and Production Engineering, Nanyang Technological University, 50 Nanyang Avenue, Singapore 639798.

E-mail address: mtyng@ntu.edu.sg (T.Y. Ng).

0022-460X/$ - see front matter © 2003 Published by Elsevier Ltd.
doi:10.1016/S0022-460X(03)00517-0

1. Introduction

Based on the actuation working principles, micropumps can be classified under a host of effects such as electromagnetic, electrostatic, piezoelectric, shape memory, etc. In the development of micropumps, it is essential to predict the performance of the micropump before the prototype is fabricated not only to save cost, but to have a better understanding of the working concepts and an idea of where potential pitfalls may occur.

Electrostatic micropumps has attracted attention in recent years since electrostatic actuators can easily be miniaturized and the electrostatic force between two capacitor plates depends upon only a few parameters such as the applied voltage, the dielectric media and the distance between the plates [1]. When a potential difference is applied across a capacitor, charges are induced on the plates of the capacitor and electrostatic forces are generated. If one plate is flexible enough to deform, the distribution of the charges on this plate varies and electrostatic force changes correspondingly with further deformation of the plate inducing charge redistribution on the surface of the plate. In the design and modelling of the electrostatic micropumps, this electro-mechanical coupling effect must be taken into consideration. To study this electro-mechanical coupling effect, the boundary element method (BEM) is often employed to evaluate the charge density and corresponding electrostatic force. The BEM was used in combination with the finite element method (FEM) to solve this coupled problem [2,3]. Currently, 1-D and 2-D static as well as 1-D dynamic problems have been studied in the literature [2,3]. When the transverse deflection of a plate structure exceeds half its thickness, geometric non-linear effects become significant [4]. In micropumps, the movable electrode plate membrane may experience large deformation and the non-linear effects cannot be neglected. The use of first order shear deformation theory (FSDT) for linear and non-linear analysis of plates can be respectively found in the literature [5,6].

In this paper, we examine the 2-D non-linear dynamic analysis of an electrostatic micropump. The geometric non-linear effect is taken into account by the introduction of von Karman strains. The BEM is used to solve the Laplace equation that evaluates the charge redistribution and the FEM is employed to solve the non-linear governing equations of motion of the electrode plate membrane. For a 1-D microtweezer, the effects of the frequency of the driving voltage has been studied [2]. It was found that when the driving frequency is close to half the first natural frequency, the microtweezer goes to a resonant vibration state. Here, the 2-D electrode plate is initially studied based via linear first order shear deformation plate theory as a first step in the simulation process. This is then extended to analysis based on von Karman type geometrically non-linear strain–displacement relationships. The amplitudes and frequencies of the driving voltage are varied and response trends are compared with that of linear analysis for qualitative changes. Finally, the effects of length-to-thickness ratio on the non-linear responses are investigated.

2. Dynamic FEM plate model for the micropump based on FSDT

The electrostatic micropump considered here is as shown in Fig. 1. Electrode 2 is fixed. As voltage is applied across the electrodes, the thin diaphragm electrode 1 deforms toward its

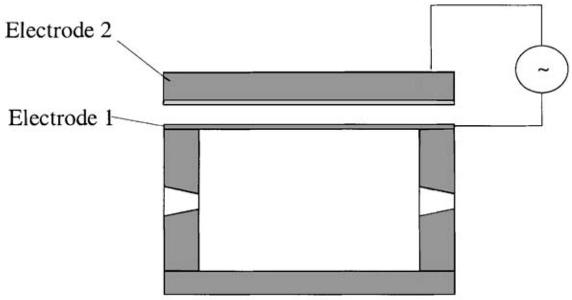

Fig. 1. Schematic of the electrostatic micropump.

counterpart electrode 2, which induces bigger volume of the pump container and fluid is thus sucked into the pump chamber. As voltage is released the diaphragm electrode 1 returns so as to squeeze the fluid out. Electrode 1 is the object to be studied and it can be simplified as a four-edge clamped thin plate.

The displacement field based on first order shear deformation plate theory is

$$\begin{aligned} &u(x,y,z,t) = u_0(x,y,z,t) + z\phi_x(x,y,t), \quad v(x,y,z,t) = v_0(x,y,z,t) + z\phi_y(x,y,t) \\ &w(x,y,z,t) = w_0(x,y,z,t), \end{aligned} \tag{1}$$

where u, v, w are displacements in the x, y, z directions, respectively, ϕ_x, ϕ_y are the rotations of a transverse normal about the x and y axes, respectively. u_0, v_0, w_0 are the midplane displacements in the x, y, z directions, respectively. The rotations can be defined as

$$\phi_x = \frac{\partial u}{\partial z}, \quad \phi_y = \frac{\partial v}{\partial z}. \tag{2}$$

Electrode 1 can be simplified as a four edge clamped plate. From first order plate theory, the governing equations can be written as

$$0 = \int_0^T \left\{ \int_{\Omega_0} \begin{bmatrix} N_{xx}\delta\varepsilon_{xx}^{(0)} + M_{xx}\delta\varepsilon_{xx}^{(1)} + N_{yy}\delta\varepsilon_{yy}^{(0)} + M_{yy}\delta\varepsilon_{yy}^{(1)} + N_{xy}\delta\gamma_{xy}^{(0)} + M_{xy}\delta\gamma_{xy}^{(1)} \\ + Q_x\delta\gamma_{xz}^{(0)} + Q_y\delta\gamma_{yz}^{(0)} - f\delta w_0 - I_0(\dot{u}_0\delta\dot{u}_0 + \dot{v}_0\delta\dot{v}_0 + \dot{w}_0\delta\dot{w}_0) \\ - I_1(\dot{\phi}_x\delta\dot{u}_0 + \dot{\phi}_y\delta\dot{v}_0 + \delta\dot{\phi}_x\dot{u}_0 + \delta\dot{\phi}_y\dot{v}_0) - I_2(\dot{\phi}_x\delta\dot{\phi}_x + \dot{\phi}_y\delta\dot{\phi}_y) \end{bmatrix} \mathrm{d}x\,\mathrm{d}y \right\} \mathrm{d}t, \tag{3}$$

where f is the uniformly distributed electrostatic load. The plate constitutive equations for the first order theories are

$$\begin{Bmatrix} N_{xx} \\ N_{yy} \\ N_{xy} \end{Bmatrix} = \begin{bmatrix} A_{11} & \upsilon A_{12} & 0 \\ \upsilon A_{12} & A_{22} & 0 \\ 0 & 0 & \dfrac{1-\upsilon}{2}A_{66} \end{bmatrix} \begin{Bmatrix} \varepsilon_{xx}^{(0)} \\ \varepsilon_{yy}^{(0)} \\ \gamma_{xy}^{(0)} \end{Bmatrix}, \tag{4}$$

$$\begin{Bmatrix} M_{xx} \\ M_{yy} \\ M_{xy} \end{Bmatrix} = \begin{bmatrix} D_{11} & \upsilon D_{12} & 0 \\ \upsilon D_{12} & D_{22} & 0 \\ 0 & 0 & \dfrac{1-\upsilon}{2} D_{66} \end{bmatrix} \begin{Bmatrix} \varepsilon_{xx}^{(1)} \\ \varepsilon_{yy}^{(1)} \\ \gamma_{xy}^{(1)} \end{Bmatrix}, \tag{5}$$

$$\begin{Bmatrix} Q_y \\ Q_x \end{Bmatrix} = K \frac{1-\upsilon}{2} \begin{bmatrix} A_{44} & 0 \\ 0 & A_{55} \end{bmatrix} \begin{Bmatrix} \gamma_{yz}^{(0)} \\ \gamma_{xz}^{(0)} \end{Bmatrix}, \tag{6}$$

where K is the shear correction factor. For an isotropic material with Young's modulus E and the Poisson ratio υ,

$$\begin{aligned} &A_{11} = \frac{Eh}{1-\upsilon^2}, \quad A_{12} = \upsilon A_{11}, \quad A_{22} = A_{11}, \\ &A_{66} = \frac{1-\upsilon}{2} A_{11}, \quad A_{44} = A_{55} = \frac{1-\upsilon}{2} K A_{11}, \\ &D_{11} = \frac{Eh^3}{12(1-\upsilon^2)}, \quad D_{12} = \upsilon D_{11}, \quad D_{22} = \upsilon D_{11}, \quad D_{66} = \frac{1-\upsilon}{2} D_{11}, \end{aligned} \tag{7}$$

$$I_i = b \int_{-h/2}^{h/2} \rho z^i \, \mathrm{d}z \quad (i = 0, 1, 2), \tag{8}$$

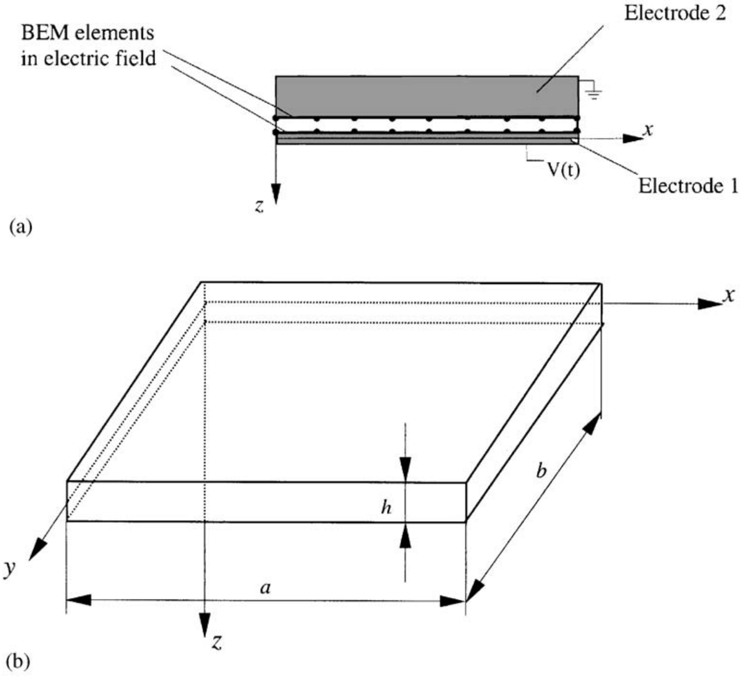

Fig. 2. (a) Boundary elements in electric field. (b) Electrode 1 and corresponding co-ordinate system.

where ρ is the density of the plate, a the length, b the width and h the thickness of the plate, see Fig. 2b. The von Karman strain–displacement relations are

$$\begin{Bmatrix} \varepsilon_{xx} \\ \varepsilon_{yy} \\ \gamma_{yz} \\ \gamma_{xz} \\ \gamma_{xy} \end{Bmatrix} = \begin{Bmatrix} \varepsilon_{xx}^{(0)} \\ \varepsilon_{yy}^{(0)} \\ \gamma_{yz}^{(0)} \\ \gamma_{xz}^{(0)} \\ \gamma_{xy}^{(0)} \end{Bmatrix} + z \begin{Bmatrix} \varepsilon_{xx}^{(1)} \\ \varepsilon_{yy}^{(1)} \\ \gamma_{yz}^{(1)} \\ \gamma_{xz}^{(1)} \\ \gamma_{xy}^{(1)} \end{Bmatrix} = \begin{Bmatrix} \dfrac{\partial u_0}{\partial x} + \dfrac{1}{2}\left(\dfrac{\partial w_0}{\partial x}\right)^2 \\ \dfrac{\partial v_0}{\partial y} + \dfrac{1}{2}\left(\dfrac{\partial w_0}{\partial y}\right)^2 \\ \dfrac{\partial w_0}{\partial y} + \phi_y \\ \dfrac{\partial w_0}{\partial x} + \phi_x \\ \dfrac{\partial u_0}{\partial y} + \dfrac{\partial v_0}{\partial x} + \dfrac{\partial w_0}{\partial x}\dfrac{\partial w_0}{\partial y} \end{Bmatrix} + z \begin{Bmatrix} \dfrac{\partial \phi_x}{\partial x} \\ \dfrac{\partial \phi_y}{\partial y} \\ 0 \\ 0 \\ \dfrac{\partial \phi_x}{\partial y} + \dfrac{\partial \phi_y}{\partial x} \end{Bmatrix}. \tag{9}$$

From Eq. (3), the Euler–Lagrange equations are obtained by setting the coefficients of $\delta u_0, \delta v_0, \delta w_0, \delta\phi_x, \delta\phi_y$ in Ω_0 to zero separately:

$$\begin{aligned}
\delta u_0 &: \frac{\partial N_{xx}}{\partial x} + \frac{\partial N_{xy}}{\partial y} = I_0 \frac{\partial^2 u_0}{\partial t^2} + I_1 \frac{\partial^2 \phi_x}{\partial t^2}, \\
\delta v_0 &: \frac{\partial N_{xy}}{\partial x} + \frac{\partial N_{yy}}{\partial y} = I_0 \frac{\partial^2 v_0}{\partial t^2} + I_1 \frac{\partial^2 \phi_y}{\partial t^2}, \\
\delta w_0 &: \frac{\partial Q_x}{\partial x} + \frac{\partial Q_y}{\partial y} + N(w_0) + f = I_0 \frac{\partial^2 w_0}{\partial t^2}, \\
\partial \phi_x &: \frac{\partial M_{xx}}{\partial x} + \frac{\partial M_{xy}}{\partial y} - Q_x = I_2 \frac{\partial^2 \phi_x}{\partial t^2} + I_1 \frac{\partial^2 u_0}{\partial t^2}, \\
\partial \phi_y &: \frac{\partial M_{xy}}{\partial x} + \frac{\partial M_{yy}}{\partial y} - Q_y = I_2 \frac{\partial^2 \phi_y}{\partial t^2} + I_1 \frac{\partial^2 v_0}{\partial t^2},
\end{aligned} \tag{10}$$

with

$$N(w_0) = \frac{\partial}{\partial x}\left(N_{xx}\frac{\partial w_0}{\partial x} + N_{xy}\frac{\partial w_0}{\partial y}\right) + \frac{\partial}{\partial y}\left(N_{xy}\frac{\partial w_0}{\partial x} + N_{yy}\frac{\partial w_0}{\partial y}\right). \tag{11}$$

The weak forms the five equations in Eq. (10) are obtained by multiplying them with $\delta u_0, \delta v_0, \delta w_0, \delta\phi_x, \delta\phi_y$ respectively, and integrating over the element domain

$$\begin{aligned}
0 = {} & \int_{\Omega^e} \left(\frac{\partial \delta u_0}{\partial x} N_{xx} + \frac{\partial \delta u_0}{\partial y} N_{xy} + I_0 \delta u_0 \frac{\partial^2 u_0}{\partial t^2} + I_1 \delta u_0 \frac{\partial^2 \phi_x}{\partial t^2} \right) \mathrm{d}x\,\mathrm{d}y \\
& - \oint_{\Gamma^e} P_x \delta u_0 \, \mathrm{d}s,
\end{aligned} \tag{12a}$$

$$0 = \int_{\Omega^e} \left(\frac{\partial \delta v_0}{\partial x} N_{xy} + \frac{\partial \delta v_0}{\partial y} N_{yy} + I_0 \delta v_0 \frac{\partial^2 v_0}{\partial t^2} + I_1 \delta u_0 \frac{\partial^2 \phi_x}{\partial t^2} \right) \mathrm{d}x\,\mathrm{d}y - \oint_{\Gamma^e} P_y \delta v_0 \,\mathrm{d}s, \tag{12b}$$

$$0 = \int_{\Omega^e} \left[\frac{\partial \delta w_0}{\partial x} Q_x + \frac{\partial \delta w_0}{\partial y} Q_y - \delta w_0 f + I_0 \delta w_0 \frac{\partial^2 w_0}{\partial t^2} \right] \mathrm{d}x\,\mathrm{d}y - \oint_{\Gamma^e} [Q_x n_x + Q_y n_y] \delta w_0 \,\mathrm{d}s, \tag{12c}$$

$$0 = \int_{\Omega^e} \left(\frac{\partial \delta \phi_x}{\partial x} M_{xx} + \frac{\partial \delta \phi_x}{\partial y} M_{xy} + \delta \phi_x Q_x + I_2 \delta \phi_x \frac{\partial^2 \phi_x}{\partial t^2} + I_1 \delta \phi_x \frac{\partial^2 u_0}{\partial t^2} \right) \mathrm{d}x\,\mathrm{d}y - \oint_{\Gamma^e} T_x \delta \phi_x \mathrm{d}s, \tag{12d}$$

$$0 = \int_{\Omega^e} \left(\frac{\partial \delta \phi_y}{\partial x} M_{xy} + \frac{\partial \delta \phi_y}{\partial y} M_{yy} + \delta \phi_y Q_y + I_2 \delta \phi_y \frac{\partial^2 \phi_y}{\partial t^2} + I_1 \delta \phi_y \frac{\partial^2 v_0}{\partial t^2} \right) \mathrm{d}x\,\mathrm{d}y - \oint_{\Gamma^e} T_y \delta \phi_y \mathrm{d}s \tag{12e}$$

in which

$$P_x \equiv N_{xx} n_x + N_{xy} n_y, \quad P_y \equiv N_{xy} n_x + N_{yy} n_y, \quad T_x \equiv M_{xx} n_x + M_{xy} n_y,$$
$$T_y \equiv M_{xy} n_x + M_{yy} n_y, \quad Q_n \equiv Q_x n_x + Q_y n_y. \tag{12f}$$

The dependent variables $u_0, v_0, w_0, \phi_x, \phi_y$ can be approximated using the Lagrange interpolation functions, i.e.,

$$u_0(x,y,t) = \sum_{j=1}^{m} u_j(t) \psi_j^e(x,y), \quad v_0(x,y,t) = \sum_{j=1}^{m} v_j(t) \psi_j^e(x,y),$$
$$w_0(x,y,t) = \sum_{j=1}^{n} w_j(t) \psi_j^e(x,y), \quad \phi_x(x,y,t) = \sum_{j=1}^{p} S_j^1(t) \psi_j^e(x,y),$$
$$\phi_y(x,y,t) = \sum_{j=1}^{p} S_j^2(t) \psi_j^e(x,y), \tag{12g}$$

where ψ_j^e are the Lagrange interpolation functions.

The quadratic Lagrange interpolation functions of rectangular elements in terms of the element co-ordinates (ξ, η) are

$$\begin{Bmatrix} \psi_1^e \\ \psi_2^e \\ \psi_3^e \\ \psi_4^e \\ \psi_5^e \\ \psi_6^e \\ \psi_7^e \\ \psi_8^e \\ \psi_9^e \end{Bmatrix} = \frac{1}{4}\begin{Bmatrix} (1-\xi)(1-\eta)(-\xi-\eta-1)+(1-\xi^2)(1-\eta^2) \\ (1+\xi)(1-\eta)(\xi-\eta-1)+(1-\xi^2)(1-\eta^2) \\ (1+\xi)(1+\eta)(\xi+\eta-1)+(1-\xi^2)(1-\eta^2) \\ (1-\xi)(1+\eta)(-\xi+\eta-1)+(1-\xi^2)(1-\eta^2) \\ 2(1-\xi^2)(1-\eta)-(1-\xi^2)(1-\eta^2) \\ 2(1+\xi)(1-\eta^2)-(1-\xi^2)(1-\eta^2) \\ 2(1-\xi^2)(1+\eta)-(1-\xi^2)(1-\eta^2) \\ 2(1-\xi)(1-\eta^2)-(1-\xi^2)(1-\eta^2) \\ 4(1-\xi^2)(1-\eta^2) \end{Bmatrix}. \tag{12h}$$

Substituting Eq. (12g) for $u_0, v_0, w_0, \phi_x, \phi_y$ into the weak forms in Eqs. (12a)–(12e), we obtain the semi-discrete finite element model of the first order theory as

$$\begin{bmatrix} [K^{11}] & [K^{12}] & [K^{13}] & [K^{14}] & [K^{15}] \\ [K^{12}]^{\mathrm{T}} & [K^{22}] & [K^{23}] & [K^{24}] & [K^{25}] \\ [K^{13}]^{\mathrm{T}} & [K^{23}]^{\mathrm{T}} & [K^{33}] & [K^{34}] & [K^{35}] \\ [K^{14}]^{\mathrm{T}} & [K^{24}]^{\mathrm{T}} & [K^{34}]^{\mathrm{T}} & [K^{44}] & [K^{45}] \\ [K^{15}]^{\mathrm{T}} & [K^{25}]^{\mathrm{T}} & [K^{35}]^{\mathrm{T}} & [K^{45}]^{\mathrm{T}} & [K^{55}] \end{bmatrix} \begin{Bmatrix} \{u^e\} \\ \{v^e\} \\ \{w^e\} \\ \{S^1\} \\ \{S^2\} \end{Bmatrix} + \begin{bmatrix} I_0[M] & [0] & [0] & I_1[M] & [0] \\ [0] & I_0[M] & [0] & [0] & I_1[M] \\ [0] & [0] & I_0[M] & [0] & [0] \\ I_1[M] & [0] & [0] & I_2[M] & [0] \\ [0] & I_1[M] & [0] & [0] & I_2[M] \end{bmatrix} \begin{Bmatrix} \{\ddot{u}^e\} \\ \{\ddot{v}^e\} \\ \{\ddot{w}^e\} \\ \{\ddot{S}^1\} \\ \{\ddot{S}^2\} \end{Bmatrix} = \begin{Bmatrix} \{F^1\} \\ \{F^2\} \\ \{F^3\} \\ \{F^4\} \\ \{F^5\} \end{Bmatrix} \tag{12i}$$

or

$$[K^e]\{\Delta^e\} + [M^e]\{\ddot{\Delta}^e\} = \{F^e\}. \tag{12j}$$

For the linear case, which means that the von Karman strains are not included, the coefficients of the submatrices $[K^{\alpha\beta}]$ and $[M^{\alpha\beta}]$ and vectors $\{F^{\alpha}\}$ are defined for $(\alpha, \beta = 1, 2, \ldots, 5)$ by the expressions

$$
\begin{aligned}
K_{ij}^{1\alpha} &= \int_{\Omega_e} \left(\frac{\partial \psi_i^e}{\partial x} N_{1j}^{\alpha} + \frac{\partial \psi_i^e}{\partial y} N_{6j}^{\alpha} \right) \mathrm{d}x\, \mathrm{d}y, \\
K_{ij}^{2\alpha} &= \int_{\Omega_e} \left(\frac{\partial \psi_i^e}{\partial x} N_{6j}^{\alpha} + \frac{\partial \psi_i^e}{\partial y} N_{2j}^{\alpha} \right) \mathrm{d}x\, \mathrm{d}y, \\
K_{ij}^{3\alpha} &= \int_{\Omega_e} \left(\frac{\partial \psi_i^e}{\partial x} Q_{1j}^{\alpha} + \frac{\partial \psi_i^e}{\partial y} Q_{2j}^{\alpha} \right) \mathrm{d}x\, \mathrm{d}y, \\
K_{ij}^{4\alpha} &= \int_{\Omega_e} \left(\frac{\partial \psi_i^e}{\partial x} M_{1j}^{\alpha} + \frac{\partial \psi_i^e}{\partial y} M_{6j}^{\alpha} + \psi_i^e Q_{1j}^{\alpha} \right) \mathrm{d}x\, \mathrm{d}y, \\
K_{ij}^{5\alpha} &= \int_{\Omega_e} \left(\frac{\partial \psi_i^e}{\partial x} M_{6j}^{\alpha} + \frac{\partial \psi_i^e}{\partial y} M_{2j}^{\alpha} + \psi_i^e Q_{2j}^{\alpha} \right) \mathrm{d}x\, \mathrm{d}y, \\
M_{ij} &= \int_{\Omega_e} \psi_i^e \psi_j^e \, \mathrm{d}x\, \mathrm{d}y.
\end{aligned}
\tag{12k}
$$

The coefficients N_{Ij}^{α}, M_{Ij}^{α}, and Q_{Ij}^{α} for $\alpha = 1, 2, \ldots, 5$ and $I = 1, 2, 6$ are given by

$$
\begin{aligned}
& N_{1j}^{1} = A_{11} \frac{\partial \psi_j^e}{\partial x}, \quad N_{1j}^{2} = A_{12} \frac{\partial \psi_j^e}{\partial y}, \quad N_{1j}^{4} = 0, \\
& N_{1j}^{5} = 0, \quad N_{2j}^{1} = A_{12} \frac{\partial \psi_j^e}{\partial x}, \quad N_{2j}^{2} = A_{22} \frac{\partial \psi_j^e}{\partial y}, \\
& N_{2j}^{4} = 0, \quad N_{2j}^{5} = 0, \quad N_{6j}^{1} = A_{66} \frac{\partial \psi_j^e}{\partial y}, \\
& N_{6j}^{2} = A_{66} \frac{\partial \psi_j^e}{\partial x}, \quad N_{6j}^{4} = 0, \quad N_{6j}^{5} = 0, \\
& M_{1j}^{1} = 0, \quad M_{1j}^{2} = 0, \quad M_{1j}^{4} = D_{11} \frac{\partial \psi_j^e}{\partial x}, \\
& M_{1j}^{5} = D_{12} \frac{\partial \psi_j^e}{\partial y}, \quad M_{2j}^{1} = 0, \quad M_{2j}^{2} = 0, \\
& M_{2j}^{4} = D_{12} \frac{\partial \psi_j^e}{\partial x}, \quad M_{2j}^{5} = D_{22} \frac{\partial \psi_j^e}{\partial y}, \quad M_{6j}^{1} = 0, \\
& M_{6j}^{2} = 0, \quad M_{6j}^{4} = D_{66} \frac{\partial \psi_j^e}{\partial y}, \quad M_{6j}^{5} = D_{66} \frac{\partial \psi_j^e}{\partial x}, \\
& N_{1j}^{3} = 0, \quad N_{2j}^{3} = 0, \quad N_{6j}^{3} = 0, \\
& M_{1j}^{3} = 0, \quad M_{2j}^{3} = 0, \quad M_{6j}^{3} = 0, \\
& Q_{1j}^{3} = 0, \quad Q_{2j}^{3} = 0,
\end{aligned}
\tag{12l}
$$

$$
\begin{aligned}
F_i^1 &= \oint_{\Gamma^e} P_x \psi_i^e \,\mathrm{d}x\,\mathrm{d}y, \quad F_i^2 = \oint_{\Gamma^e} P_y \psi_i^e \,\mathrm{d}x\,\mathrm{d}y,\\
F_i^3 &= \oint_{\Gamma^e} f \psi_i^e \,\mathrm{d}x\,\mathrm{d}y + \oint_{\Gamma^e} Q_n \psi_i^e \,\mathrm{d}s,\\
F_i^4 &= \oint_{\Gamma^e} T_x \psi_i^e \,\mathrm{d}x\,\mathrm{d}y, \quad F_i^5 = \oint_{\Gamma^e} T_y \psi_i^e \,\mathrm{d}x\,\mathrm{d}y.
\end{aligned}
\tag{12m}
$$

Finite element model is established with nine-node quadratic element. If the von Karman strains are to be included in the finite element model, the following non-linear equation could be obtained [7]:

$$[K^e]\{\bar{\Delta}^e\} + [M^e]\{\ddot{\bar{\Delta}}^e\} = \{F^e\}, \tag{13a}$$

where $[M^e]$ is the mass matrix of element for the first order shear deformation plate theory defined in Eq. (12k) and $[K^e]$ is the stiffness matrix of element including geometric non-linear effect. The additional stiffness coefficients $[\bar{K}^{\alpha 3}]$ ($\alpha = 1, 2, 3$), which are defined by Eq. (13b), are to be added to the corresponding linear coefficients defined in Eq. (12k) so as to form the stiffness matrix $[K^e]$ for the non-linear case

$$
\begin{aligned}
\bar{K}_{ij}^{13} &= \frac{1}{2}\int_{\Omega_e}\left(\frac{\partial \psi_i}{\partial x}\bar{N}_{1j} + \frac{\partial \psi_i}{\partial y}\bar{N}_{6j}\right)\mathrm{d}x\,\mathrm{d}y, \quad \bar{K}_{ij}^{23} = \frac{1}{2}\int_{\Omega_e}\left(\frac{\partial \psi_i}{\partial x}\bar{N}_{6j} + \frac{\partial \psi_i}{\partial y}\bar{N}_{2j}\right)\mathrm{d}x\,\mathrm{d}y,\\
\bar{K}_{ij}^{31} &= \int_{\Omega_e}\left(\bar{N}_{1i}\frac{\partial \psi_j}{\partial x} + \bar{N}_{6i}\frac{\partial \psi_j}{\partial y}\right)\mathrm{d}x\,\mathrm{d}y = 2\bar{K}_{ji}^{13}, \quad \bar{K}_{ij}^{32} = \int_{\Omega_e}\left(\bar{N}_{6i}\frac{\partial \psi_j}{\partial x} + \bar{N}_{2i}\frac{\partial \psi_j}{\partial y}\right)\mathrm{d}x\,\mathrm{d}y = 2\bar{K}_{ji}^{23},\\
\bar{K}_{ij}^{33} &= \int_{\Omega_e}\left[\frac{\partial \psi_i}{\partial x}\left(\bar{N}_1\frac{\partial \psi_j}{\partial x} + \bar{N}_6\frac{\partial \psi_j}{\partial y}\right) + \frac{\partial \psi_i}{\partial y}\left(\bar{N}_6\frac{\partial \psi_j}{\partial x} + \bar{N}_2\frac{\partial \psi_j}{\partial y}\right)\right]\mathrm{d}x\,\mathrm{d}y,
\end{aligned}
\tag{13b}
$$

$$
\begin{aligned}
\bar{N}_{\beta j} &= A_{\beta 1}\frac{\partial w_0}{\partial x}\frac{\partial \psi_j}{\partial x} + A_{\beta 2}\frac{\partial w_0}{\partial y}\frac{\partial \psi_j}{\partial y} + A_{\beta 6}\left(\frac{\partial w_0}{\partial x}\frac{\partial \psi_j}{\partial y} + \frac{\partial w_0}{\partial y}\frac{\partial \psi_j}{\partial x}\right),\\
\bar{N}_{\beta} &= \frac{1}{2}\left[A_{1\beta}\left(\frac{\partial w_0}{\partial x}\right)^2 + A_{2\beta}\left(\frac{\partial w_0}{\partial y}\right)^2 + 2A_{6\beta}\frac{\partial w_0}{\partial x}\frac{\partial w_0}{\partial y}\right] \quad (\beta = 1, 2, 6)
\end{aligned}
\tag{13c}
$$

in which, $A_{16} = A_{26} = A_{61} = A_{62} = 0$, for an isotropic material. It should be noted that the stiffness matrix $[K^e]$ is not symmetric for the non-linear case because $\bar{K}_{ij}^{3\alpha} = 2\bar{K}_{ii}^{\alpha 3}$, $\alpha = 1, 2$.

The fully discretized equations are given by

$$[\hat{K}^e(\bar{\Delta}^e)]_{s+1}\{\bar{\Delta}^e\}_{s+1} = \{\hat{F}^e\} \tag{13d}$$

and following Newmark time discretization [7]

$$
\begin{aligned}
\lfloor \hat{K}^e \rfloor_{s+1} &= [K^e]_{s+1} + \Phi[M^e]_{s+1},\\
\{\hat{F}^e\} &= \{F^e\}_{s+1} + [M^e]_{s+1}\{\ddot{\tilde{\Delta}}^e\},
\end{aligned}
\tag{13e}
$$

where $\Phi = 2/\Psi(\Delta t_s)^2$ with $\Delta t_s = t_{s+1} - t_s$ being the s time step and Ψ is an integration parameter constant defined by the scheme used.

3. Charge density and electrostatic force

As a voltage is applied onto the undeformed conductive plates, electrical charges are induced on the surface of the plate, and these charges induce surface normal pressures which constitute the electrostatic load p. In this work, electric stray field and corner effects will not been considered. As one electrode plate is flexible enough to deform under this electrostatic load, the deformed plate induces redistribution of surface charges on it and further deformation of this plate. This electromechancial coupling effect can be illustrated as

$$\begin{tikzcd}
\phi(x,y,z(w(x,y,t))) \arrow[r] & q(x,y,z(w(x,y,t))) \arrow[d] \\
w(x,y,t) \arrow[u] & p(x,y,z(w(x,y,t))) \arrow[l]
\end{tikzcd}$$

where ϕ is the electrostatic potential, q the surface charge density, p the electrostatic load and w the transverse deflection at point (x, y, z).

The electrostatic load can be calculated by

$$p(x,y) = -\frac{1}{2}\frac{q^2(x,y,z(w))}{\varepsilon}\mathbf{n}, \tag{14a}$$

where $\mathbf{n}$ is the inward normal to the conductor, ε is the dielectric constant of the medium in which the plate is placed and the charges distributed on the plate surface satisfy [8]

$$q(x,y) = \varepsilon\frac{\partial\phi(x,y,z(w))}{\partial\mathbf{n}}. \tag{14b}$$

The electrostatic potential ϕ, in the region exterior to the conductor, satisfies Laplace's equation

$$\frac{\partial^2\phi}{\partial x^2} + \frac{\partial^2\phi}{\partial y^2} + \frac{\partial^2\phi}{\partial(z(w))^2} = 0. \tag{14c}$$

Eq. (14c) is solved using the Galerkin-based boundary element method. The electric field and boundary elements is illustrated in Fig. 2a. There are mixed boundary conditions. The potential of the top surface (electrode 2) is taken to be zero, and the potential of the bottom plate (electrode 1) is the applied voltage. The potential gradient of all the other four side surfaces are zero.

4. Solution of dynamical equations

In this work, for the coupled mechanical and electrostatic field analysis, a weak coupling approach has been employed, whereby the computational mechanical and electrostatic analyses are run alternately and the effects from one is incorporated into the other repeatedly and sequentially. This weak coupling is conducted after the dynamic evolution, as opposed to the strong iteration method which provides for coupling during the dynamic step. The non-linear algebraic equations (13d) are solved by Newton's iterative method. The Newton's iterative method is based on the tangent stiffness matrix, which is symmetric for all structural problems. Suppose that the solution at the ith iteration, $\{\Delta\}^i$, is known, then let

$$\{R\} \equiv [\hat{K}]\{\Delta\} - \{\hat{F}\} = 0 \tag{15a}$$

and the solution at the $(i+1)$th iteration is given by

$$\{\Delta\}^{i+1} = \{\Delta\}^i + \{\delta\Delta\}, \tag{15b}$$

where $\{\delta\Delta\}$ is the solution increment and we have

$$\{\delta\Delta\} = -([\hat{K}(\{\Delta\}^i)]^{tan})^{-1}\{R\}^i = ([\hat{K}(\{\Delta\}^i)]^{tan})^{-1}(\{\hat{F}\} - [\hat{K}(\{\Delta\}^i)]\{\Delta\}^i), \tag{15c}$$

where $[\hat{K}(\{\Delta\}^i)]^{tan}$ is the tangent stiffness matrix and can be obtained as

$$[\hat{K}(\{\Delta\}^i)]^{tan} \equiv \left[\frac{\partial\{R\}}{\partial\{\Delta\}}\right] \text{ evaluated at } \{\Delta\} = \{\Delta\}_i. \tag{15d}$$

The iteration process is continued by solving Eq. (15c) until the convergence criteria of Eq. (15e) is satisfied. The error criterion [7] is of the form

$$\sqrt{\frac{\sum_{I=1}^{N}|\Delta_I^{i+1} - \Delta_I^i|^2}{\sum_{I=1}^{N}|\Delta_I^{i+1}|^2}} < err \quad (\text{say } 10^{-3}), \tag{15e}$$

where N is the total number of nodal generalized displacements in the finite element mesh, and *err* is the error tolerance.

5. Simulation results

For the plate membrane, i.e., electrode 1 of Fig. 1, its dimensions are taken to be 1000 μm × 1000 μm × 50 μm and the distance between the two electrodes is 750 μm, unless otherwise explicitly defined. The material properties are that of aluminum with Young's modulus $E =$ 70 GPa, density $\rho = 2600$ kg/m^3 and the Poisson ratio $\upsilon = 0.25$.

5.1. Non-linear load–deflection relationship

The response of the plate under uniformly distributed load is studied examined here and Fig. 3 shows the load–deflection curve. The geometric non-linearity is included by introducing the von Karman strain–displacement relations resulting in the clearly non-linear load–deflection profile.

5.2. Effects of driving frequency—linear plate analysis

Based on linear plate analysis, the first natural frequency of the plate is found to be $\omega_1 = 2.7 \times 10^6$ rad/s. Fig. 4(a) shows the dynamic responses of the plate driven by voltages of $V = 4.0\sin(62.8t)V/8.0\sin(62.8t)V$. It is observed that a stable response is obtained even though the driving frequency is as low as 10 Hz. Fig. 4(b) is the dynamic response of the plate driven by voltages of $V = 4.0\sin(\omega_1 t)V/8.0\sin(\omega_1 t)V$. It can be seen that as the plate is excited by a harmonic wave with a frequency equal to the first natural frequency of the plate, the plate has stable dynamic response. This is because the force is in effect proportional to the square of V, and

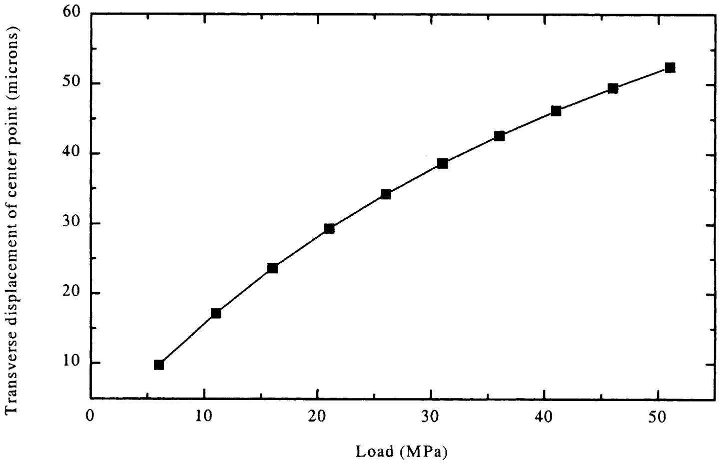

Fig. 3. Non-linear load–deflection relationship of the plate under uniformly distributed load.

the frequency of the dynamic response is thus expected to be twice that of the frequency of the applied voltage.

Fig. 4(c) shows the dynamic response of the plate driven by voltages of $V = 4.0\sin(\omega_1 t/2)V/8.0\sin(\omega_1 t/2)V$. It is observed that as the driving frequency is equal to half of the fundamental frequency of the plate, the plate goes into a resonant state. This trend for the 2-D linear plate analysis is similar to that observed by Shi et al. [2] in a 1-D analysis of a microtweezer. Figs. 4(d) and 4(e) are the dynamic responses of the plate driven by the voltages of $V = 4.0\sin(0.95\omega_1 t)V/8.0\sin(0.95\omega_1 t)V$ and $V = 4.0\sin(1.05\omega_1 t)V/8.0\sin(1.05\omega_1 t)V$, respectively. It can be seen that when the driving frequencies are close to half of the fundamental frequency of the plate, the dynamic responses have especially large amplitudes. This is again in line with the observations of Shi et al. [2] for a 1-D analysis of a microtweezer. Fig. 4(f) presents the dynamic response of the plate driven by voltages of $V = 4.0\sin(1.5\omega_1 t)V/8.0\sin(1.5\omega_1 t)V$. It is noted that a stable response is obtained as the driving frequency is sufficiently clear of half of the fundamental frequency of the plate.

5.3. Effects of driving frequency—non-linear plate analysis

Fig. 5 presents the corresponding results via non-linear plate analysis of the results presented in Fig. 4. Figs. 5(a) and 5(b) show the dynamic responses of the plate membrane excited by voltages of $V = 4.0\sin(62.8t)V/8.0\sin(62.8t)V$ and $V = 4.0\sin(\omega_1 t)V/8.0\sin(\omega_1 t)V$, respectively. Comparing this with corresponding results of Figs. 4(a) and (b), it is observed the response amplitudes when using non-linear analysis are lower. In Fig. 5(c), where the plate is driven by voltages of $V = 4.0\sin(\omega_1 t/2)V/8.0\sin(\omega_1 t/2)V$, we observe qualitatively different results corresponding to the linear case of Fig. 4(c) in that there is no resonant phenomena.

In Figs. 5(d) and 5(e) which are the dynamic responses of the plate driven by voltages of $V = 4.0\sin(0.95\omega_1 t)V/8.0\sin(0.95\omega_1 t)V$ and $V = 4.0\sin(1.05\omega_1 t)V/8.0\sin(1.05\omega_1 t)V$, respectively, it is further observed that there are no large amplitude responses that were obtained by linear analysis in Figs. 4(d) and 4(e). Fig. 5(f) shows the response of the plate driven by voltages of

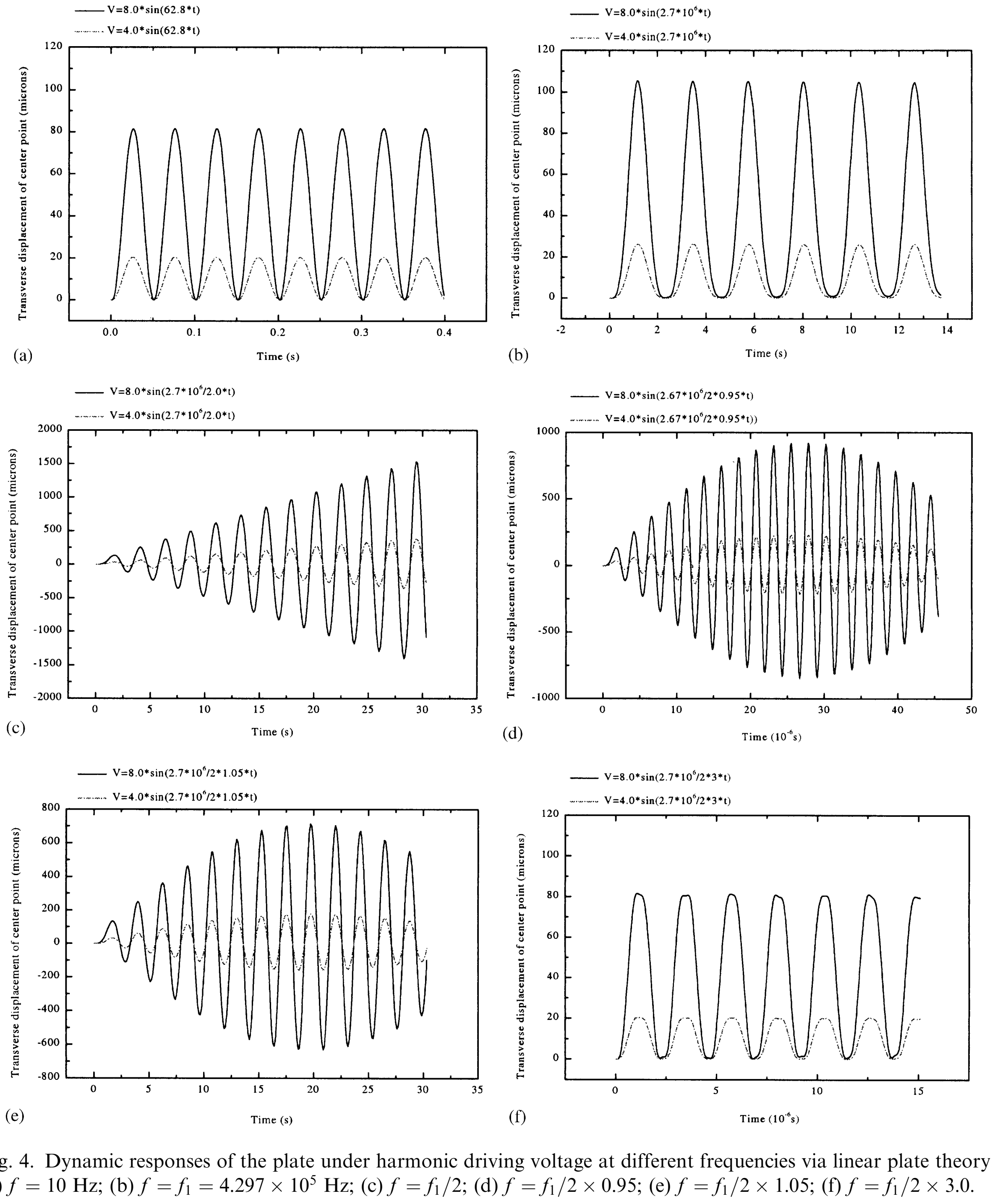

Fig. 4. Dynamic responses of the plate under harmonic driving voltage at different frequencies via linear plate theory. (a) $f = 10$ Hz; (b) $f = f_1 = 4.297 \times 10^5$ Hz; (c) $f = f_1/2$; (d) $f = f_1/2 \times 0.95$; (e) $f = f_1/2 \times 1.05$; (f) $f = f_1/2 \times 3.0$.

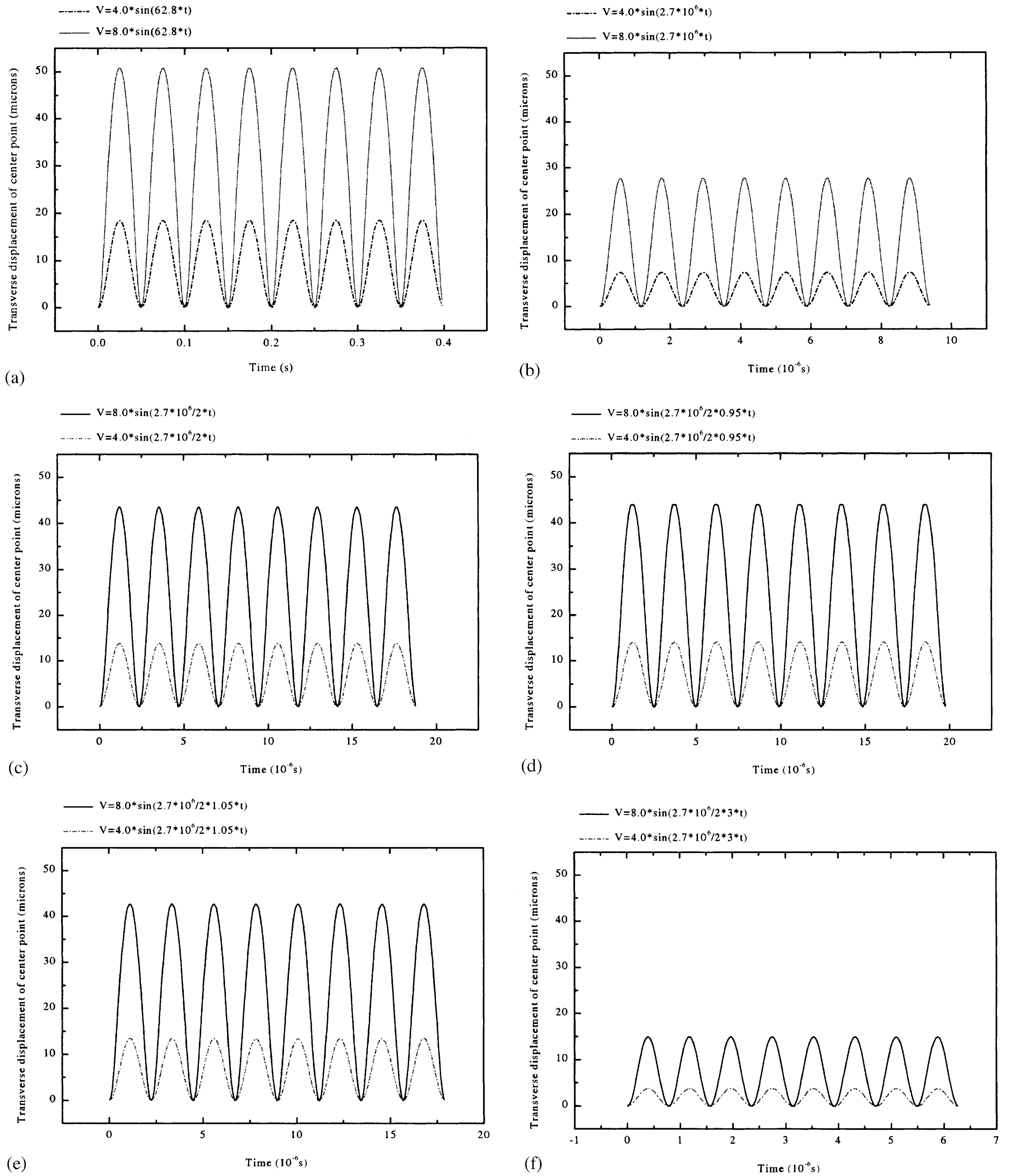

Fig. 5. Dynamic responses of the plate under harmonic driving voltage at different frequencies via non-linear plate theory. (a) $f = 10$ Hz; (b) $f = f_1 = 4.297 \times 10^5$ Hz; (c) $f = f_1/2$; (d) $f = f_1/2 \times 0.95$; (e) $f = f_1/2 \times 1.05$; (f) $f = f_1/2 \times 3.0$.

$V = 4.0\sin(1.5\omega_1 t)V/8.0\sin(1.5\omega_1 t)V$. Again, as in Figs. 5(a) and 5(b), it is observed here in Fig. 5(f) that the response amplitudes when using non-linear analysis are lower in comparison with results of Fig. 4(f). Thus apart from resonant and near-resonant cases, linear plate analysis generally over estimates the amplitude responses. These qualitative and quantitative differences can be expected based on previous works on free and forced large deflection vibrations of thin plates [4,9,10].

5.4. Influence of amplitude of the applied voltage

Fig. 6 illustrates the variation of the dynamic response of the plate at various harmonic voltage amplitudes of 4.0, 8.0, 12.0 and 20.0 V at a frequency of 10 Hz. In Fig. 6(a), it can be seen that when the voltage amplitude is low at 4.0 V, the response amplitude of the plate is relatively small at 20 μm. As this response amplitude is within the applicability range of linear theory, it is not

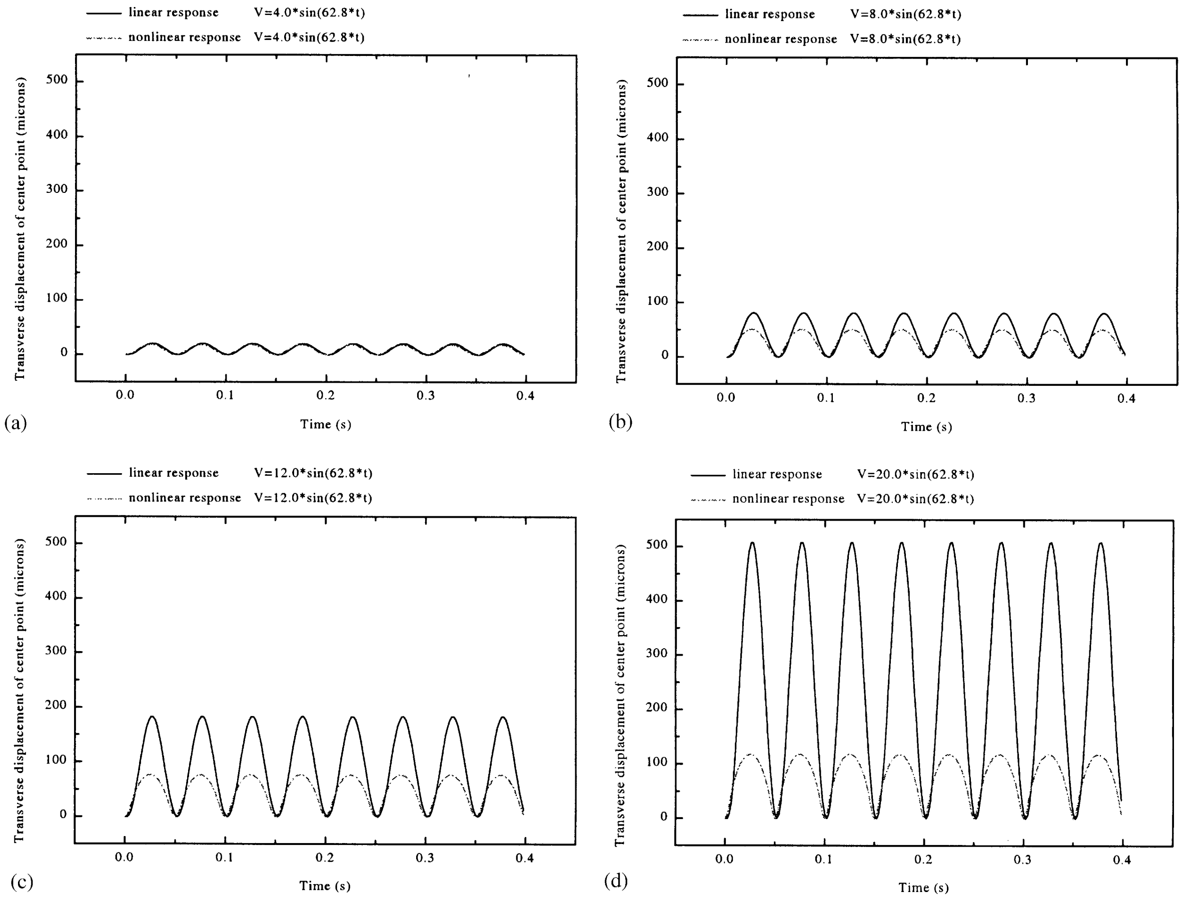

Fig. 6. Comparison of dynamic responses of the plate under harmonic driving voltages of different amplitudes. (a) Dynamic response of the plate under voltage 4.0 sin(62.8*t*); (b) 8.0 sin(62.8*t*); (c) 12.0 sin(62.8*t*); (d) 20.0 sin(62.8*t*).

surprising to find that both results from linear and non-linear plate theory are almost coincident. As the voltage amplitude is increased to 8.0 V in Fig. 6(b), the non-linear response is about 50 μm and the linear response is about 75 μm. However, as the response exceeds half the thickness of the plate, linear plate theory is no longer reliable thus resulting in the differences in the response amplitudes. As the voltage amplitude is further increased to 12.0 and 20.0 V (Figs. 6(c) and 6(d)), the expected divergence of the linear and non-linear results are clearly observed.

5.5. *Influence of plate thickness*

The effect of variation of the plate thickness is examined here by varying the length-to-thickness (a/h) ratio, Fig. 7. The driving voltage is $8.0\sin(62.8t)$. When the plate is relatively thick with $a/h = 10$, i.e., $h = 100$ μm, the response amplitude is around 15 μm. As this is within the applicability range of linear plate theory, it is observed that both sets of results from linear and non-linear plate theory show excellent agreement. When thickness is reduced to $a/h = 20$, i.e.,

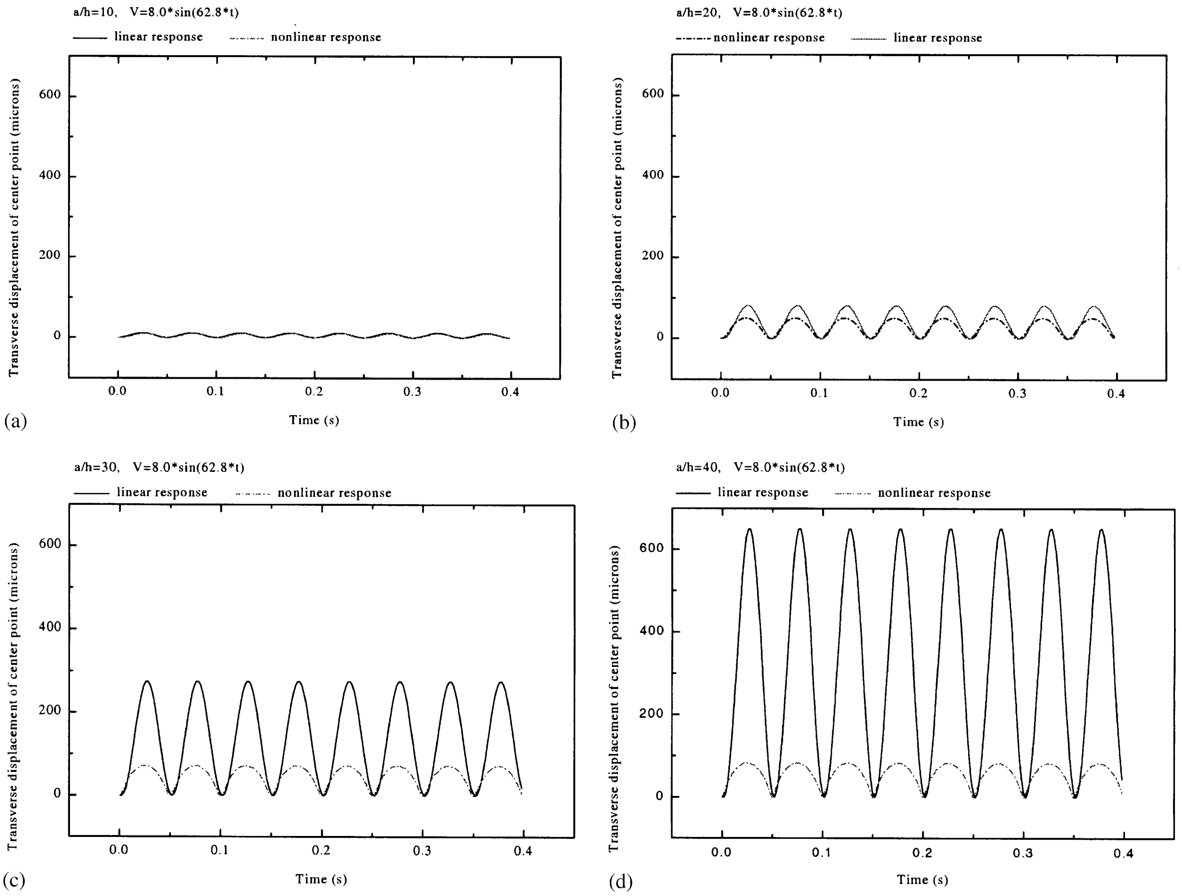

Fig. 7. Dynamic responses of the plate at various length-to-thickness ratios. (a) $a/h = 10$; (b) $a/h = 20$; (c) $a/h = 30$; (d) $a/h = 40$.

$h = 50$ μm, discrepancies are observed as linear plate theory begins to over predict the amplitude. Further reduction in the thickness clearly exposes the inadequacy of linear plate theory for large deformation prediction.

6. Conclusions

The non-linear dynamic analysis of an electrostatic micropump has been presented. Coupled electro-mechanical effects are considered in the evaluation of the micropump where the BEM was employed to solve the quasi 3-D Laplace equation governing the electrostatics. FSDT is used to model the electrode membrane and geometric non-linearity was present due to the inclusion of von Karman strains. The FEM was employed to discretize the governing equations which were solved by Newton's iteration method. Linear plate theory results were also generated for comparison. Results showed that when using linear plate theory, trends for the 2-D linear plate analysis were similar to that observed by Shi et al. [2] in a 1-D analysis for a microtweezer. However, when corresponding results were generated using non-linear plate theory, results were qualitatively and quantitatively different. Parametric studies with respect to the driving voltage amplitude and plate thickness have been presented. All results point to the necessity for consideration of geometric non-linearity in this application.

Appendix A. Nomenclature

a, b	plate length and width
A_{ij}	extensional stiffness
D_{ij}	bending stiffness
E	Young's modulus
F^e	force vector entry
h	plate thickness
I_0, I_1, I_2	mass moments of inertia
$K_{ij}^{\alpha\beta}$	stiffness matrix entry
$M_{ij}^{\alpha\beta}$	mass matrix entry
M_{xx}, M_{xy}, M_{yy}	moment resultants
n_x, n_y	unit outward normal vectors
N_{xx}, N_{xy}, N_{yy}	in-plane force resultants
p	electrostatic load
q	surface charge density
Q_x, Q_y	transverse force resultants
u, v, w	displacements in the x, y, z directions
u_0, v_0, w_0	midplane displacements in the x, y, z directions
ε	dielectric constant
$\varepsilon_{xx}, \varepsilon_{yy}$	normal strains
$\gamma_{xy}, \gamma_{xz}, \gamma_{yz}$	shear strains
ϕ	electrostatic potential

ϕ_x, ϕ_y	transverse normal rotations
υ	The Poisson ratio
Ω^e, Γ^e	elemental surface area and boundary range
ψ_i^e	Lagrange interpolation functions
Δ^e	displacement vector entry
Φ, Ψ	Newmark integration parameters

References

[1] S. Fatikow, U. Rembold, *Microsystems Technology and Microrobotics*, Springer, Berlin, Heidelberg, New York, 1997.

[2] F. Shi, P. Ramesh, S. Mukherjee, Dynamic analysis of micro-electro-mechanical systems, *International Journal for Numerical Methods in Engineering* 39 (1996) 4119–4319.

[3] M. Kaltenbacher, H. Landes, R. Lerch, F. Lindinger, A finite-element/boundary-element method for the simulation of coupled electrostatic-mechanical systems, *Journal de Physique III* 7 (1997) 1975–1982.

[4] W. Han, M. Petyt, Geometrically nonlinear vibration analysis of thin, rectangular plates using the hierarchical finite element method—I: the fundamental mode of isotropic plates, *Computers and Structures* 63 (1997) 295–308.

[5] Z.Q. Cheng, S. Kitipornchai, Exact bending solution of inhomogeneous plates from homogeneous thin-plate deflection, *American Institute of Aeronautics and Astronautics Journal* 38 (2000) 1289–1291.

[6] P.C. Dumir, S. Joshi, G.P. Dube, Geometrically nonlinear axisymmetric analysis of thick laminated annular plate using FSDT, *Composites Part B—Engineering* 32 (2001) 1–10.

[7] J.N. Reddy, *Mechanics of Laminated Composite Plates—Theory and Analysis*, CRC Press, Boca Raton, New York, London, Tokyo, 1997.

[8] J.D. Jackson, *Classical Electrodynamics*, 2nd Edition, Wiley, Singapore, 1975.

[9] M. Chuh Mei, D.U. Kamolphan, A finite element method for nonlinear forced vibrations of rectangular plates, *American Institute of Aeronautics and Astronautics Journal* 23 (1985) 1104–1110.

[10] R. Benamar, M.M.K. Bennouna, The effects of large vibration amplitudes on the mode shapes and natural frequencies of thin elastic structures, Part III: fully clamped rectangular isotropic plates-measurements of the mode shape amplitude dependence and the spatial distribution of harmonic distortion, *Journal of Sound and Vibration* 175 (1994) 377–395.